

Article

Effect of Laser Shock Peening on the Passivation Behavior of Subtractively and Additively Manufactured Ti–6Al–4V Alloys in pH 2 Buffer Solution

JuHee Lee ¹, Jan Kaufman ², Martin Divoký ², Tomáš Mocek ², Jan Brajer ² and HeeJin Jang ^{1,*}

¹ Department of Advanced Materials Engineering, Chosun University, 309 Pilmundaero, Dong-gu, Gwangju 61452, Republic of Korea

² HiLASE Centre, Institute of Physics of the Czech Academy of Sciences, Za Radnicí 828, 252 41 Dolní Břežany, Czech Republic; jan.kaufman@hilase.cz (J.K.)

* Correspondence: heejin@chosun.ac.kr

Abstract

The effects of laser shock peening (LSP) on subtractively manufactured (SM) and additively manufactured (AM) Ti–6Al–4V alloys in pH 2 buffer solution were investigated. LSP increased the surface roughness from $0.25 \pm 0.05 \mu\text{m}$ to $0.6 \pm 0.1 \mu\text{m}$, raised Vickers hardness by 12–16%, and introduced compressive residual stresses of 400–950 MPa. Microstructural analysis indicated that LSP promoted β -phase formation and grain refinement in SM alloys, while reducing the α' -phase fraction in AM alloys. Electrochemical testing revealed that all LSP-treated specimens exhibited active–passive transitions, unlike the stable passive response of unpeened samples. The corrosion rate (i_{corr}) decreased from approximately 5×10^{-6} to $1 \times 10^{-6} \text{ A} \cdot \text{cm}^{-2}$ after LSP. During 24 h potentiostatic polarization at $1.3 V_{\text{SCE}}$, the passive current density stabilized at 10^{-8} – $10^{-7} \text{ A} \cdot \text{cm}^{-2}$, with LSP AM specimens exhibiting values approximately twice those of their unpeened counterparts. Mott–Schottky analysis confirmed that the donor density (N_D) in the SM alloy changed negligibly after LSP, indicating a stable passive alloy. In contrast, the N_D for the AM alloy increased from 1×10^{19} to $3 \times 10^{19} \text{ cm}^{-3}$, suggesting an oxygen-vacancy-rich, less stable passive film. Overall, LSP reduces the corrosion rate primarily through the introduction of compressive residual stress but may impair the long-term passive-film stability of AM Ti–6Al–4V owing to defect generation. In contrast, the SM alloy maintains passive-film stability under identical treatment conditions.

Keywords: corrosion; Mott–Schottky; Ti–6Al–4V; additive manufacturing; laser shock peening



Academic Editor: Antonio Riveiro

Received: 10 February 2026

Revised: 21 March 2026

Accepted: 25 March 2026

Published: 3 April 2026

Copyright: © 2026 by the authors.

Licensee MDPI, Basel, Switzerland.

This article is an open access article distributed under the terms and

conditions of the [Creative Commons Attribution \(CC BY\)](https://creativecommons.org/licenses/by/4.0/) license.

1. Introduction

Additive manufacturing (AM), also referred to as three-dimensional (3D) printing [1], is a promising technology for customizable and smart production, offering benefits such as the ability to manufacture complex shapes inaccessible to conventional techniques and reduced material costs. However, AM processes suffer from various problems, such as residual stresses, solidification defects, and uneven surface conditions arising from rapid temperature changes [2,3]. Post-processing and process-optimization strategies are typically required to mitigate these issues.

Ti alloys are widely used in the aerospace and biomedical industries owing to their low weight, excellent mechanical properties, and high corrosion resistance [4–7]. Notably, the

mechanical performance of Ti alloys is strongly governed by microstructural features such as grain size, dislocation density, and interfacial characteristics [8]. Because of their high cost and difficulty in machining, Ti alloys are particularly suitable for AM processing [9]. Accordingly, various researchers have focused on the material properties of Ti alloys subjected to AM [10–13].

In addition, Ti and its alloys are passive metals that form a thin protective TiO_2 film on their surfaces [14]. As in the case of other passive alloys, exposure to halogen ions can lead to localized breakdown of the passive film, resulting in localized corrosion and stress corrosion cracking (SCC) [15–18]. Several studies have reported that Ti alloys fabricated using AM are less corrosion resistant than those fabricated using subtractive manufacturing (SM) employing conventional casting and forging techniques [19–22]. This inferior resistance is largely attributable to the growth of stress corrosion cracks, promoted by the presence of pores and voids [21], or the tensile residual stresses introduced during the AM process. Therefore, numerous engineering approaches have been explored to eliminate pores, voids, and residual stresses in AM alloys [23–26].

Several mechanical surface modification techniques, including conventional shot peening (SP) [27], ultrasonic shot peening (USP) [28,29] and ultrasonic nanocrystal surface modification (UNSM) [30,31] have been investigated to enhance the mechanical and corrosion properties of metallic materials. These techniques induce compressive residual stresses and grain refinement near the surface, improving fatigue performance, wear resistance [32,33], pitting resistance [34,35], hardness, and corrosion resistance in both stainless steels and Ti alloys [36–38]. However, such surface modification processes involve repeated mechanical impacts or ultrasonic vibrations, which are often accompanied by localized temperature rises and potential surface contamination, making it difficult to completely exclude thermal or environmental effects during processing.

In contrast, laser shock peening (LSP) [39–41] employs high-intensity laser-induced shock waves to generate compressive residual stresses that can extend several hundred micrometers beneath the surface, with minimal thermal effects. Consequently, LSP has been shown to effectively inhibit fatigue cracking and SCC [42,43], as well as to improve resistance to uniform [36,44,45] and pitting corrosion [46,47] in various materials. Despite these advantages, the mechanisms by which LSP influences the passive film characteristics of AM Ti–6Al–4V alloys remain poorly understood.

Because the corrosion resistance of Ti alloys is primarily controlled by the stability and electrochemical properties of the passive oxide film, understanding the passivation behavior of Ti–6Al–4V alloys is essential for clarifying the corrosion mechanisms of AM materials. The passivation behavior of Ti–6Al–4V alloys is governed by the properties of the TiO_2 -based passive film, which behaves as an n-type semiconductor in which oxygen vacancies act as electron donors [48,49]. Mott–Schottky studies on SM Ti–6Al–4V have reported donor densities on the order of 10^{20} m^{-3} , varying with film formation potential [50]. In AM Ti–6Al–4V alloys, however, the dominance of metastable α' martensite and reduced β -phase content result in a thinner and less stable passive film, associated with higher passive current densities and greater susceptibility to film dissolution [51–54]. These findings underscore that passive film breakdown—serving as the precursor to both pitting corrosion and SCC—is critically sensitive to the AM-induced microstructure, highlighting the importance of systematically investigating passivation behavior in AM Ti–6Al–4V alloys.

The corrosion resistance of passive alloys is influenced not only by macroscopic defects such as pores and voids but also by the intrinsic stability of the passive film. According to the point defect model [55], the stability and localized failure of passive films are determined by the formation, migration, and dissipation of point defects within the film. Because point defect characteristics govern the semiconducting behavior of passive films, Mott–Schottky

analysis has been widely employed to evaluate the electrochemical stability of passive alloys, particularly in SM materials [56,57].

Although recent years have witnessed increasing research on the corrosion behavior of AM alloys, studies on the point defect characteristics of AM passive films remain limited. Existing work has primarily focused on stainless steel, Ti–6Al–4V, and Ni-based alloys [58–60], with findings suggesting that AM alloys exhibit a higher density of point defects than their SM counterparts. This increase in defect concentration has been linked to higher passive current density and greater susceptibility to pitting corrosion [58,59]. Despite these insights, there exists an urgent need to comprehensively examine point defects in AM Ti–6Al–4V passive films to elucidate the impact of AM processing on the corrosion mechanisms of passive metals and alloys [60].

However, directly examining the effects of point defects in AM passive films remains challenging, as traditional bulk polarization techniques provide limited insight into the localized evolution of point defects in microstructurally complex alloys. Recently, advanced electrochemical techniques, such as dynamic electrochemical impedance spectroscopy, the scanning vibrating electrode technique, and scanning electrochemical microscopy, have been applied to investigate localized electrochemical activity and passive film heterogeneity at the microscale [61,62]. While these advanced techniques provide valuable insight into the nanoscale distribution of defects, they do not directly quantify the overall defect concentration or charge transport mechanisms within passive films. Therefore, complementary electrochemical approaches, particularly Mott–Schottky analysis, remain essential for evaluating the semiconductor properties of passive films and for understanding their passivation behavior.

Considering these aspects, this study clarifies the passivation behavior of AM Ti–6Al–4V alloys from a physicochemical perspective by linking the point defect characteristics of passive films with microstructural and electrochemical responses. To this end, the point defect properties of passive films formed on AM alloys were systematically investigated and directly compared with those of conventionally wrought (SM) alloys. In addition, the effects of LSP on the microstructure and electrochemical behavior of both alloys were examined. This approach provides new insight into the role of AM-induced microstructures in governing passivity and defect chemistry in Ti–6Al–4V alloys.

2. Experimental Procedures

2.1. Sample Preparation

SM Ti–6Al–4V alloy sheets and AM Ti–6Al–4V bars were used as the experimental specimens. The SM material was a commercially available hot-rolled Ti–6Al–4V plate with a nominal Ti–6Al–4V composition (Al \approx 6 wt.%, V \approx 4 wt.%). The AM Ti–6Al–4V alloy was fabricated via direct energy deposition (DED) (InssTek, Inc., Daejeon, Republic of Korea). The chemical composition of the Ti–6Al–4V alloy used in the DED process was as follows: Ti bal., C 0.01%, O 0.13%, N 0.02%, H 0.002%, Fe 0.2%, Al 6.62%, and V 4%, with each other element $<$ 0.1%. The total content of other elements was below 0.4%. The DED process was performed using a beam size of 1200 μ m and laser power of 500–812 W. The powder feeding rate was maintained at 3 g·min^{−1}, and the carrier gas flow rate (Ar) was set as 3.4 L·min^{−1}. The tool path followed a zigzag pattern. The specimens were cut into pieces sized 50 mm \times 35 mm \times 2 mm. The AM test pieces were extracted along the planes perpendicular to the build direction (BD specimens) and transverse to the build plane (TD specimen).

2.2. LSP Sample Preparation

LSP samples were prepared using laser pulses generated from the first stage of the power amplifier of a Bivoj Laser, a Yb:YAG laser system operating at a wavelength of 1030 nm and repetition rate of 10 Hz [63]. The pulses had a duration of 10 ns with a rectangular temporal profile. Prior to the treatment, the samples were covered with a 100- μm -thick black vinyl tape to protect the surface against thermal effects. Laminar water flow (approximately 1 mm) was applied to confine the plasma to the sample. Laser pulses with an energy of 2 J were focused onto a 2 mm laser spot, resulting in a specific energy density (fluence) of $63.7 \text{ J}\cdot\text{cm}^{-2}$ and power density of $5 \text{ GW}\cdot\text{cm}^{-2}$. To prevent the tape from tearing, the pulses were delivered in a layer consisting of four sequences. Each sequence adopted a laser pattern with 0% overlap between individual laser spots, and successive sequences were shifted by 1 mm in the X, Y, and XY directions on the exposed surface to achieve a 50% laser spot overlap within the treated layer.

2.3. Microstructure Analysis and Hardness Measurement

To examine the alloy microstructure, specimens were ground using SiC papers up to 4000 grit and finished with a 1 μm alumina paste. The prepared specimens were observed using optical microscopy (OM, AMIO, ZEISS, Jena, Germany). For more detailed microstructural characterization, scanning electron microscopy (SEM, SU-8600, Hitachi, Tokyo, Japan) was conducted at an accelerating voltage of 15 kV to examine the microstructural changes induced by LSP in the SM and AM specimens. Before OM and SEM observation, the specimen surfaces were etched using Keller's reagent for 30 s. Phase identification was performed using X-ray diffraction (XRD, Empyrean, Malvern Panalytical, Almelo, The Netherlands). Surface residual stresses in the LSP specimens were measured by XRD using the $\sin^2 \psi$ method with a Rigaku AutoMATE II X-ray diffractometer (Tokyo, Japan) and Cr K α radiation ($\lambda = 2.2897 \text{ \AA}$). These measurements were performed in two perpendicular directions relative to the laser peening direction.

The surface hardness was measured using a Vickers hardness tester (HVM-G, Shimadzu Corporation, Kyoto, Japan) with a load of 2 kgf applied for 10 s at five points on each sample surface. Surface roughness measurements (SJ-210, Mitutoyo, Kawasaki, Japan) were performed using a contact-type roughness meter along five randomly selected lines (length of 6 mm) on the surface.

2.4. Electrochemical Tests

Potentiodynamic polarization, potentiostatic polarization, and Mott–Schottky tests were performed sequentially using a potentiostat (VMP-3, Bio-Logic, Seyssinet-Pariset, France). Prior to electrochemical testing, the working electrodes were prepared as follows: Unpeened specimens were ground using SiC paper up to 2000 grit, rinsed with distilled water and ethanol, and dried in air. LSP specimens were used as is, without polishing, to preserve the shock-induced surface morphology. All specimens were mounted in epoxy resin, leaving an exposed surface area of 0.5 cm^2 . All current densities were normalized to this geometric surface area without surface roughness correction. A high-density carbon rod and saturated calomel electrode (SCE) were used as the counter and reference electrodes, respectively. The electrolyte was a pH 2 buffer solution ($18 \pm 2 \text{ }^\circ\text{C}$) that was degassed with ultrapure nitrogen gas for 1 h. This solution was prepared by mixing 975 mL of solution 1 ($0.2 \text{ M H}_3\text{BO}_3 + 0.05 \text{ M H}_8\text{C}_6\text{O}_7\cdot\text{H}_2\text{O}$) with 25 mL of solution 2 ($0.1 \text{ M NaPO}_4\cdot 12\text{H}_2\text{O}$). This acidic condition was chosen because it promotes partial dissolution of the passive film on Ti, enabling more sensitive evaluation of LSP-induced changes in passivation behavior.

After stabilization at the open circuit potential for 1800 s, potentiodynamic polarization was performed from $-1.0 V_{\text{SCE}}$ to $1.3 V_{\text{SCE}}$ at a scan rate of $1 \text{ mV}\cdot\text{s}^{-1}$. Upon reaching

1.3 V_{SCE} , potentiodynamic polarization was performed at this potential for 24 h to allow the passivation film to stabilize. Mott–Schottky analysis was then performed using staircase potentiodynamic electrochemical impedance spectroscopy. The potential was decreased from 1.3 V_{SCE} to $-1.0 V_{SCE}$ at a rate of approximately $0.1 V \cdot s^{-1}$. At each potential, the system was stabilized for 5 s before measurement. An AC amplitude of 10 mV and a frequency of 1 kHz were applied during the measurements.

3. Results and Discussion

3.1. Microstructure, Hardness, and Residual Stress Characterization

Figure 1 shows the XRD patterns obtained from the specimen surface before and after LSP treatment. For the SM specimen (Figure 1a), diffraction peaks corresponding to the α and β phases were observed. After LSP, the intensity of the β (110) peak at 39.5° increased, and a β (220) peak appeared at 82.6° . The increase in β phase intensity may be associated with stress-induced $\alpha \rightarrow \beta$ phase transformation, in which the accumulated compressive stress is partially relaxed through the formation of the β phase. The β phase has more active slip systems than the α phase, enabling more effective accommodation of the LSP-induced deformation [64]. For the AM specimens (Figure 1b,c), only α and martensitic α' phase peaks were identified both before and after LSP.

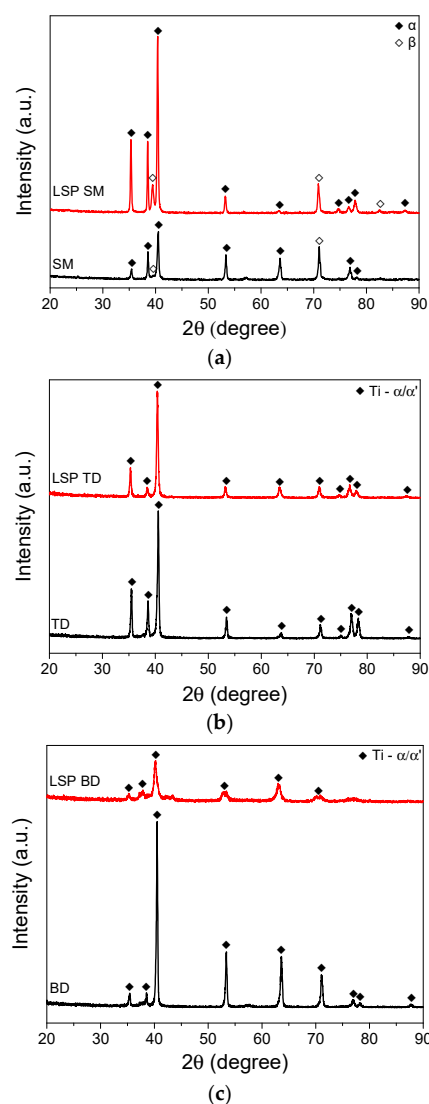


Figure 1. XRD patterns of (a) SM, (b) TD, and (c) BD specimens before and after LSP.

The cross-sectional microstructures observed in the SM and AM alloys using OM are presented in Figures 2 and 3, respectively. The SM alloys (Figure 2a,b) consisted of $\alpha + \beta$ phases, consistent with the XRD patterns (Figure 1a). After LSP (Figure 2b), the grains near the surface appeared to be deformed and refined compared with those in the unpeened sample (Figure 2a). Grains in the region extending from the surface to 40 μm were finer than those in deeper regions. In the region between 30 μm and 50 μm , the grains appeared severely deformed, whereas below 60 μm , the microstructure was similar to that of the unpeened specimen. Grain refinement has been commonly observed in shot peening [65–67] and LSP processes [36,68,69]. A previous study [70] reported that the average size of the α phase decreased from approximately 10 μm to 0.5 μm after LSP. In the present study, the grain size of the unpeened Ti–6Al–4V alloy was 5–8 μm , which, after LSP, decreased to 3–4 μm in the region extending from the surface to 40 μm . At a depth of 40–60 μm , the deformed grains exhibited horizontal and vertical dimensions of 15–25 μm and 2–3 μm , respectively. To further investigate the LSP-induced microstructural changes observed by OM, SEM observations were conducted for the LSP-treated SM and AM TD specimens. The corresponding images are presented in Figure 4. As shown in Figure 4a, the LSP-treated SM specimen exhibited a more refined and compressed microstructure near the surface compared with that in deeper regions, consistent with the grain refinement observed by OM.

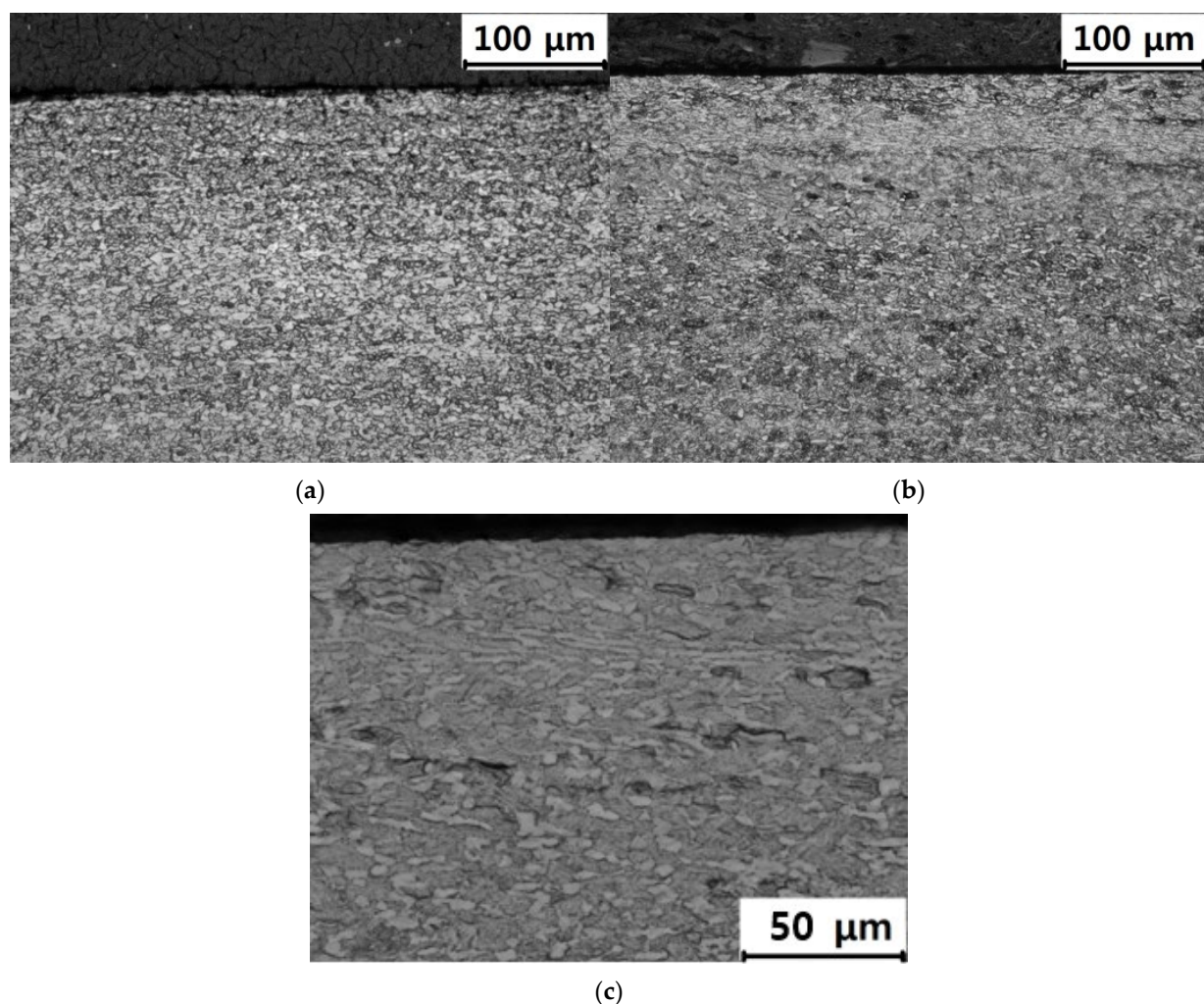


Figure 2. Cross-sectional microstructures of (a) unpeened SM Ti–6Al–4V ($\times 200$), (b) SM Ti–6Al–4V with LSP ($\times 200$), and (c) SM Ti–6Al–4V with LSP ($\times 500$).

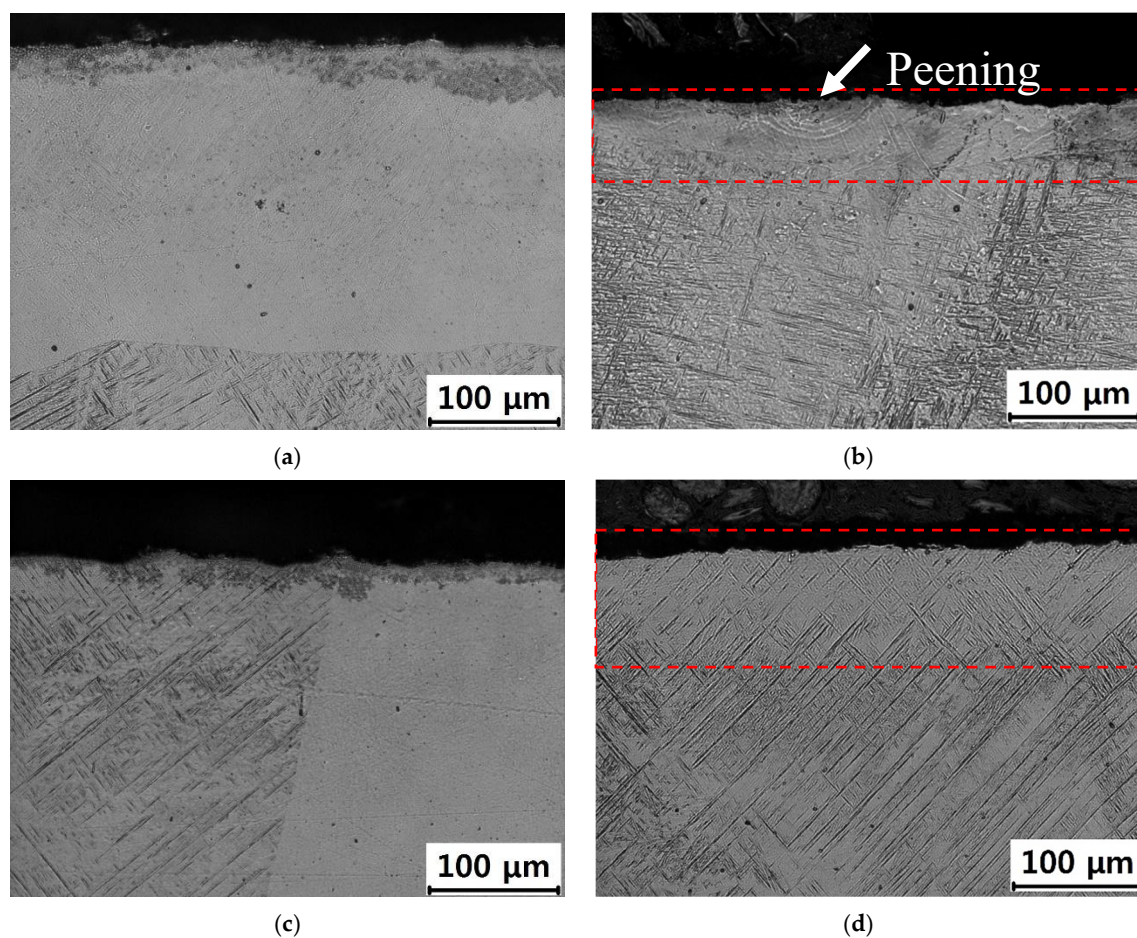


Figure 3. Cross-sectional microstructures of (a) Ti-6Al-4V TD, (b) LSP Ti-6Al-4V TD, (c) Ti-6Al-4V BD, and (d) LSP Ti-6Al-4V BD specimens.

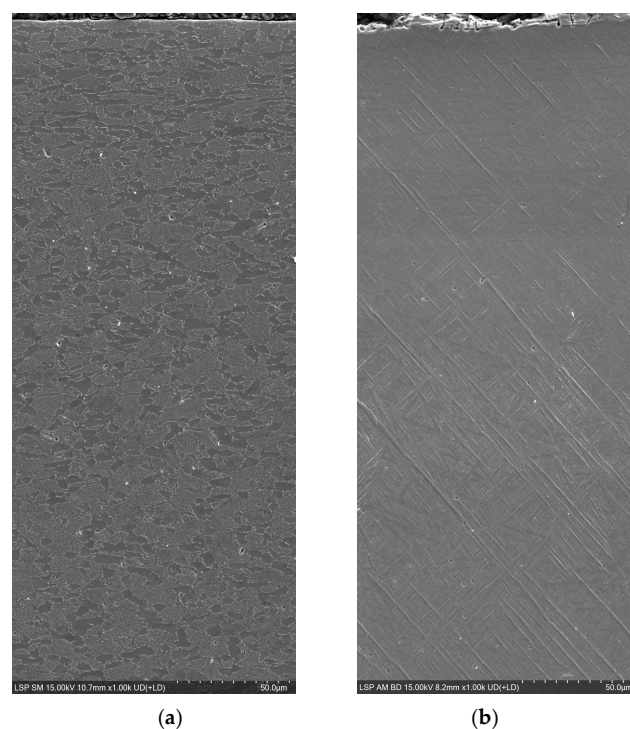


Figure 4. SEM microstructures showing the microstructural changes induced by LSP in (a) SM and (b) AM TD specimens.

In the case of the AM Ti–6Al–4V alloy, both the BD and TD specimens showed alternating light and dark regions containing the acicular martensite α' phase (Figure 3). Such light and dark areas are commonly observed in AM Ti alloys, attributable to the rapid cooling and heating cycles involved in the DED process [71]. Regions that experience different cooling rates develop distinct microstructures, resulting in noticeable differences in appearance. Additionally, process parameters such as laser power, scanning speed, and layer thickness influence the thermal history of the material, thereby affecting the microstructural evolution and contributing to the formation of light and dark regions. In this study, LSP treatment resulted in shockwave marks sized several tens of micrometers (Figure 3b) with a spacing of 1 mm. The acicular α' phase was partially fragmented and eliminated by LSP, with this effect being more pronounced near the shockwave marks (Figure 3b) and in the shallow subsurface region (Figure 3d). These changes could not be detected by XRD (Figure 1b,c) as this technique cannot distinguish between the α and α' phases owing to their identical hexagonal close-packed (HCP) crystal structure. The strong shockwaves of LSP are thus thought to fragment the brittle α' phase or cause stress-induced phase transformation. For the AM TD specimen, SEM observation of the LSP sample (Figure 4b) confirmed the partial disappearance and fragmentation of the acicular martensitic α' phase from the surface to a depth of approximately 100 μm , consistent with the OM results.

LSP resulted in an increase in surface roughness (R_a), as shown in Figure 5. Specifically, the R_a of the LSP-treated samples was 0.5–0.7 μm , more than twice those of the unpeened specimens (0.2–0.3 μm). This increase in roughness at the macroscale is attributable to the periodic indentations produced at the shock impact points, as shown in Figure 5b. Nevertheless, no significant changes in the surface profiles were observed at the microscopic scale (Figures 2 and 3).

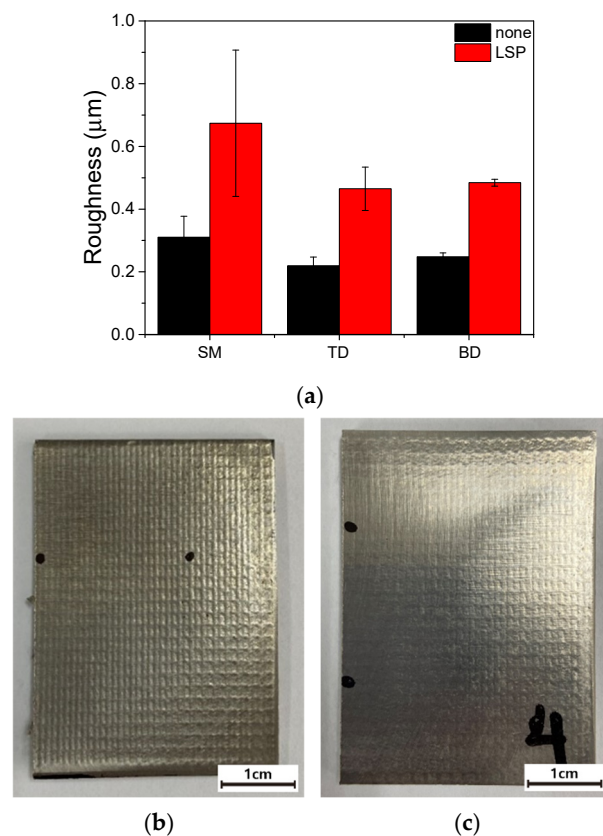


Figure 5. (a) Surface roughness (R_a) of the LSP and unpeened samples. (b) Macro-image of the LSP SM sample. (c) Macro-image of the LSP AM sample.

As expected, LSP treatment resulted in an increase in surface hardness (Figure 6, *y*-axis). The hardness of the unpeened specimens was 310–340 HV, whereas that of the LSP specimens was 370–390 HV. In general, LSP results in a high density of dislocations near the surface, leading to microstructural refinement and increased hardness [39,72–74]. The hardness increment observed in the present study was 12–16%, consistent with the work of Nalla et al. [75], who reported a hardness increase exceeding 10% following LSP.

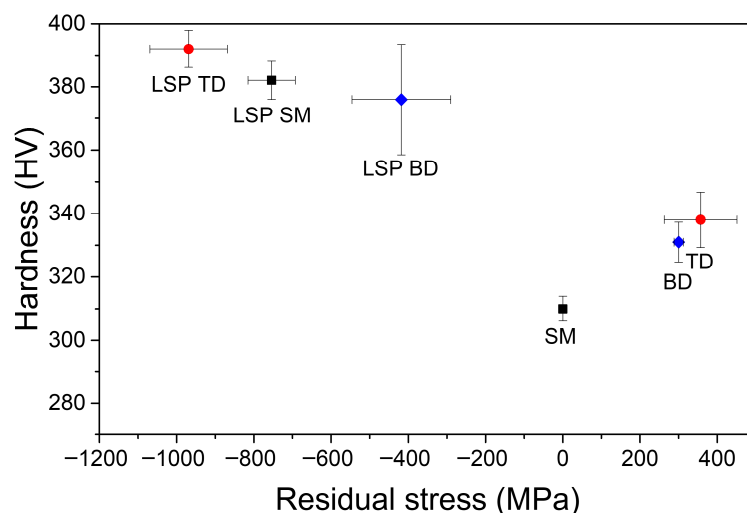


Figure 6. Effects of LSP on surface hardness and surface residual stress in SM and AM Ti–6Al–4V alloys.

This increase in hardness is associated with the effects of the residual stress [76], grain size, and dislocation concentration. Figure 6 shows that the hardness increased with increasing residual stress, regardless of whether the residual stress was tensile or compressive. All LSP specimens showed a high compressive residual stress of 400–950 MPa. In contrast, the AM specimens initially exhibited tensile residual stress of approximately 300 MPa before the LSP treatment (Figure 6, *x*-axis). The tensile residual stress in AM samples is mainly ascribed to the shrinkage of the material as the melt pool solidifies [77,78]. These results demonstrate that LSP is highly effective in inducing compressive stress in materials, consistent with numerous reports that have highlighted improvements in cracking and fatigue resistance following LSP [2,36,40,42,46,72–74,79].

The compressive residual stress in the SM specimen after LSP was not greater than that in the AM specimens. Notably, the SM alloy did not exhibit tensile residual stress before LSP. Additionally, the compressive residual stress in the TD specimen after LSP was considerably higher than that of the BD specimen, even though both specimens exhibited similar tensile stress values before LSP. These results indicate that LSP treatment is highly effective in alleviating tensile stress. However, the magnitude of the compressive stress retained after LSP does not depend solely on the initial stress state. Instead, the surface phases (light and dark regions in Figure 3) and plane direction relative to the build direction influence the effectiveness of the LSP in inducing compressive stress.

3.2. Electrochemical Characterization

Figure 7 presents the electrochemical polarization curves of the SM and AM Ti–6Al–4V alloys measured in a pH 2 buffer solution before and after LSP. The unpeened SM alloy showed highly stable passive behavior, with a passive current density below 10^{-5} A·cm⁻² and no anodic current peaks. The TD and BD AM alloys also showed passive behavior similar to that of the SM alloy, except for the value of the corrosion potential.

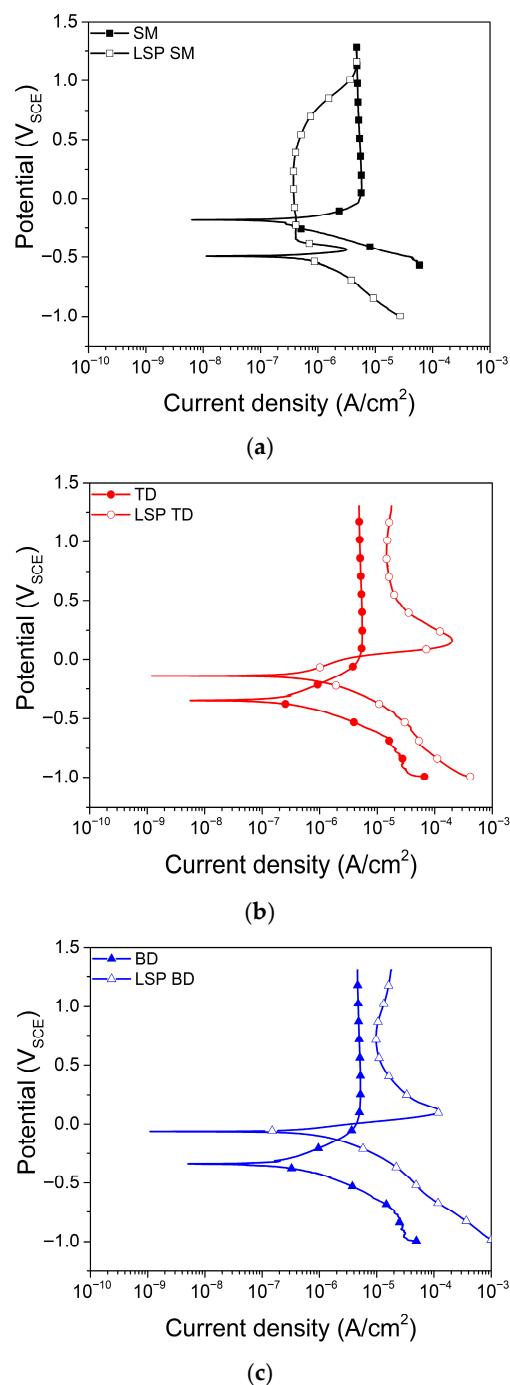


Figure 7. Potentiodynamic polarization curves for (a) SM Ti-6Al-4V, (b) AM Ti-6Al-4V (TD), and (c) AM Ti-6Al-4V (BD) alloys before and after LSP, measured in a pH 2 buffer solution.

All LSP-treated specimens (SM, TD, and BD) exhibited an active–passive transition, whereas the unpeened specimens remained in the passive region. The critical anodic current density of the LSP SM specimen was approximately $3 \times 10^{-6} \text{ A} \cdot \text{cm}^{-2}$, and its passive current density was lower than $10^{-6} \text{ A} \cdot \text{cm}^{-2}$ at potentials below $0.5 \text{ V}_{\text{SCE}}$ (Figure 7a). According to the Pourbaix diagram [80], the anodic current peak at approximately $-0.5 \text{ V}_{\text{SCE}}$ is attributable to the oxidation of Ti^{2+} to Ti^{3+} which may become thermodynamically feasible under the influence of LSP-induced residual stress and lattice distortions. The anodic current peak at approximately $0\text{--}0.2 \text{ V}_{\text{SCE}}$ observed in the AM alloys is attributed to the oxidation of V^{3+} to V^{4+} (VO^{2+}), reflecting the dissolution of supersaturated V in the martensitic α' phase [75]. This process is further promoted by LSP-induced residual

stress and increased dislocation density, which act as diffusion pathways for metal-ion dissolution. At potentials above $0.5 V_{SCE}$, the passive current density increased in all LSP-treated specimens, corresponding to the oxidation of V^{4+} to V^{5+} , as indicated by the Pourbaix diagram.

In this study, i_{corr} was determined using different approaches depending on the electrochemical behavior of each specimen. For LSP-treated specimens, which exhibited a clear active–passive transition, i_{corr} was estimated by Tafel extrapolation. For unpeened specimens, which showed stable passive behavior without a distinct active region, the current density at $0.5 V_{SCE}$ was used as a measure of corrosion rate, as Tafel extrapolation was not applicable [81]. In the unpeened condition, the i_{corr} values of the AM specimens (TD and BD) were comparable to that of the unpeened SM specimen, all being of the order of $5 \times 10^{-6} A \cdot cm^{-2}$. After LSP treatment, i_{corr} decreased for all specimens and remained of the order of $\sim 10^{-6} A \cdot cm^{-2}$ (Figure 8b). This reduction in i_{corr} is closely associated with the introduction of compressive residual stress by LSP process, which has been widely reported to suppress anodic dissolution and localized corrosion processes by reducing the effective driving force for corrosion reactions [82].

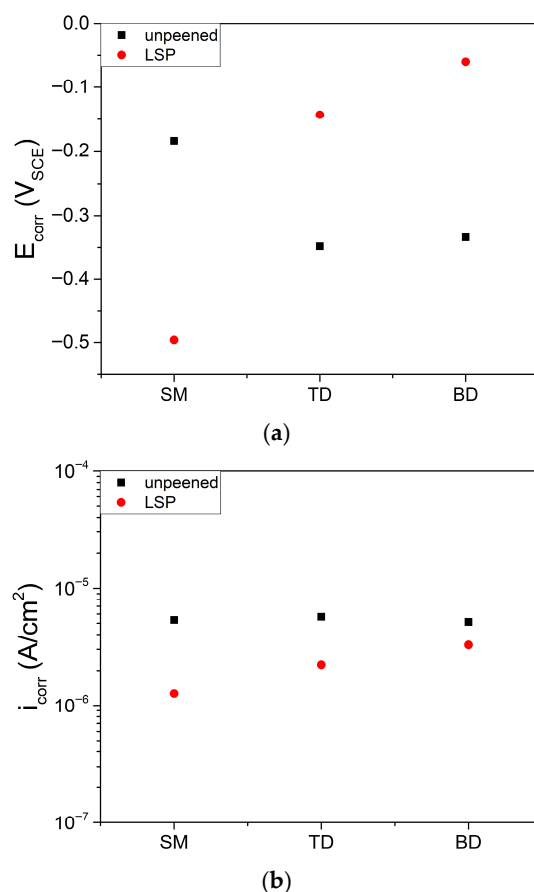


Figure 8. Corrosion (a) potential and (b) current density determined from potentiodynamic polarization curves. For LSP-treated specimens, i_{corr} was estimated by Tafel extrapolation. For unpeened specimens, the current density at $0.5 V_{SCE}$ was used as i_{corr} .

In the case of the AM alloy, although the LSP-treated specimens exhibited slightly higher current densities than the unpeened specimens in the passive region above the corrosion potential (E_{corr}), this behavior did not considerably influence the initial i_{corr} value. This observation suggests that the inhibitory effect of compressive residual stress on early-stage anodic dissolution outweighs potential adverse contributions from localized V dissolution.

Previous studies have reported that increasing the β -phase fraction enhances the corrosion resistance of Ti–6Al–4V alloys, whereas the martensitic α' phase is generally more susceptible to corrosion [51–53,83]. In the present study, despite partial decomposition of the martensitic α' phase induced by LSP (Figures 3 and 4b, and Section 3.1), the i_{corr} value was observed to decrease.

The surface roughness after LSP increased by approximately twofold, as shown in Figure 5a and discussed in Section 3.1. Although increased surface roughness is generally associated with accelerated corrosion [84–87], the i_{corr} in the present study either decreased or remained nearly unchanged after LSP. While direct quantitative comparison with results obtained in different environments is not feasible, these findings highlight that the detrimental effect associated with increased surface roughness could be offset by LSP-induced factors such as compressive residual stress and limited β -phase formation.

At 1.3 V_{SCE} , 24 h potentiostatic polarization (Figure 9a) showed that the current density decreased over time and approached a steady-state value. The LSP AM and LSP SM specimens displayed the highest and lowest initial current densities, respectively. This trend is consistent with the final passive current density (i_{pass}) obtained from the potentiodynamic polarization curves (Figure 7). After 24 h, the unpeened SM, LSP SM, and unpeened AM samples reached steady-state passive current densities (i_{ss}) within the 10^{-8} – 10^{-7} A·cm $^{-2}$ range. The LSP AM specimen retained a higher i_{ss} than its unpeened counterpart.

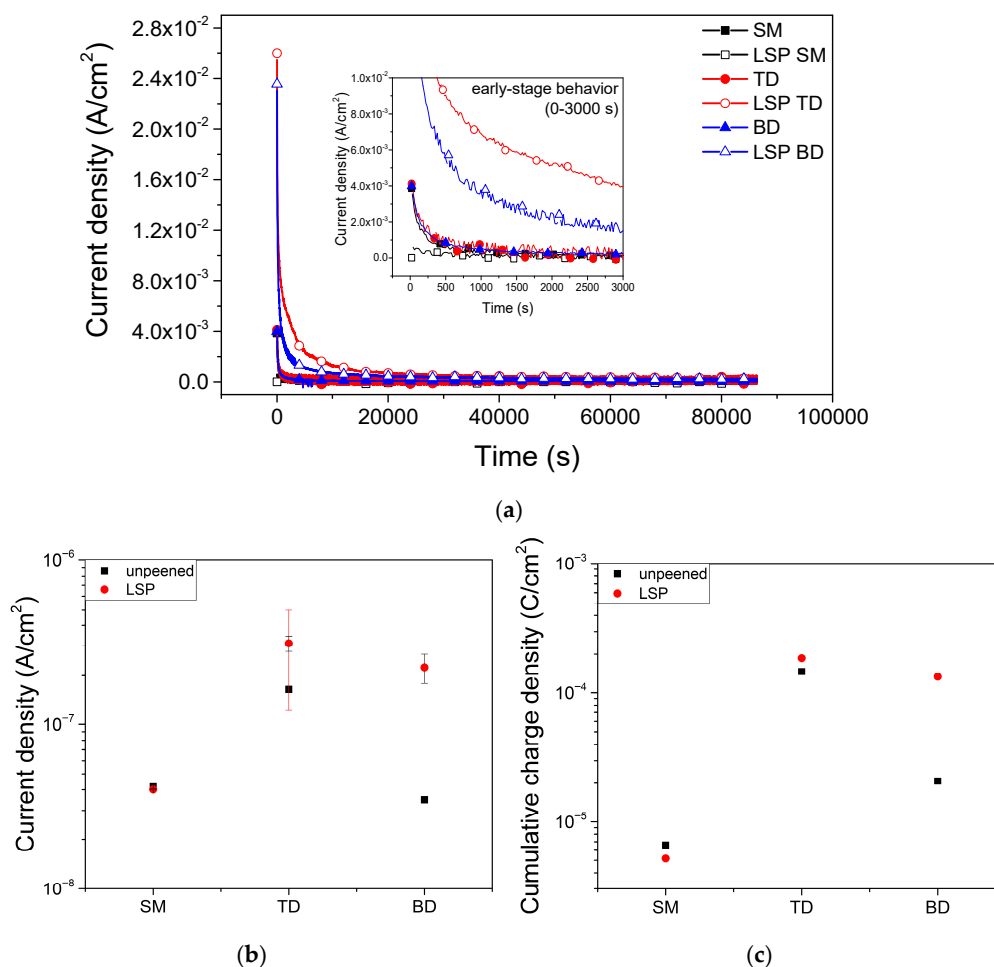


Figure 9. (a) Passive current density transient at 1.3 V_{SCE} for 24 h, (b) average current density in the last 600 s, and (c) cumulative charge density integrated over the last 600 s in a pH 2 buffer solution.

This electrochemical behavior correlates well with the microstructures. In the SM alloy, LSP led to grain refinement and a slight increase in the β phase (Figures 1a and 2b). This

refined microstructure accelerated the initial formation of the passive film, as reflected by the decreased i_{ss} at early stages (Figure 9a). However, i_{ss} changed little after 24 h (Figure 9b), indicating that although microstructural refinement accelerates early passivation, it exerts a limited impact on the long-term stability of the passive film.

In contrast, the AM alloy was dominated by a martensitic α' phase with notable build-layer boundaries and pores (Figures 1b,c, 3 and 4b). Zhan et al. [54] reported that, owing to the presence of an α' matrix, a minor β phase, and high porosity, laser powder bed fusion Ti–6Al–4V develops a thinner and less stable passive film than cast Ti–6Al–4V, resulting in a passivation current density approximately an order of magnitude higher. Consistent with these findings, the unpeened AM in the present study already exhibited higher i_{ss} than the SM specimens, and i_{ss} further increased after LSP. This behavior suggests that α' -phase-dominated microstructures promote the formation of defect-rich passive films with reduced long-term stability.

The cumulative charge density (Q_{final}), shown in Figure 9c and calculated over the final 600 s of the 24 h potentiostatic polarization period, provides a quantitative measure of the electrochemical activity under near-steady-state conditions. Among the tested specimens, the LSP SM alloy exhibited a Q_{final} value of $5.17 \times 10^{-6} \text{ C}\cdot\text{cm}^{-2}$, comparable to that of the unpeened SM ($6.59 \times 10^{-6} \text{ C}\cdot\text{cm}^{-2}$), indicating that LSP does not adversely affect the long-term passivation stability of the SM alloy and may slightly improve it. In contrast, the AM specimens showed substantially higher Q_{final} values, ranging from $2.08 \times 10^{-5} \text{ C}\cdot\text{cm}^{-2}$ to $1.86 \times 10^{-4} \text{ C}\cdot\text{cm}^{-2}$, reflecting increased charge consumption during the later stages of passivation. These results suggest that differences in cumulative charge behavior are associated with variations in microstructure and the resulting defect characteristics of the passive film.

A Mott–Schottky analysis was performed to assess the semiconducting properties of the passive film. The Mott–Schottky plot of the film grown at 1.3 V for 24 h (Figure 10a) exhibits the characteristics of an n-type semiconductor, which is typical of passive films on Ti alloys [48,49]. For n-type semiconductors, the donor density (N_d) and flat-band potential (E_{FB}) can be obtained as

$$\frac{1}{C^2} = \frac{2}{\epsilon\epsilon_0 e N_d} \left(E - E_{FB} - \frac{kT}{e} \right), \quad (1)$$

where C is the capacitance of the space-charge layer; ϵ is the dielectric constant of the passive film, which is approximately 85 for a Ti alloy [50]; ϵ_0 is the dielectric constant in vacuum ($8.854 \times 10^{-14} \text{ F}\cdot\text{cm}^{-1}$); e is the electric charge of an electron ($1.602 \times 10^{-19} \text{ C}$); E is the applied potential; k is the Boltzmann constant ($1.38 \times 10^{-23} \text{ J}\cdot\text{K}^{-1}$); and T is the temperature in K. It should be noted that the dielectric constant of Ti-based passive films can vary widely depending on film composition, structure and formation conditions [50], and therefore the calculated N_d values should be interpreted in a comparative sense rather than as absolute values.

E_{FB} decreased with LSP treatment (Figure 10b). In general, E_{FB} of TiO_2 is influenced by the crystalline polymorph, crystalline orientation, and morphology, all of which can be influenced by the film synthesis or growth procedure [88]. According to the literature, E_{FB} of TiO_2 in a pH 2 aqueous solution ranges from approximately -0.3 to 0 V_{NHE} and decreases with increasing anatase fraction. However, these data could not be directly compared with the present data owing to differences in the composition and surface conditions of the samples used in both studies.

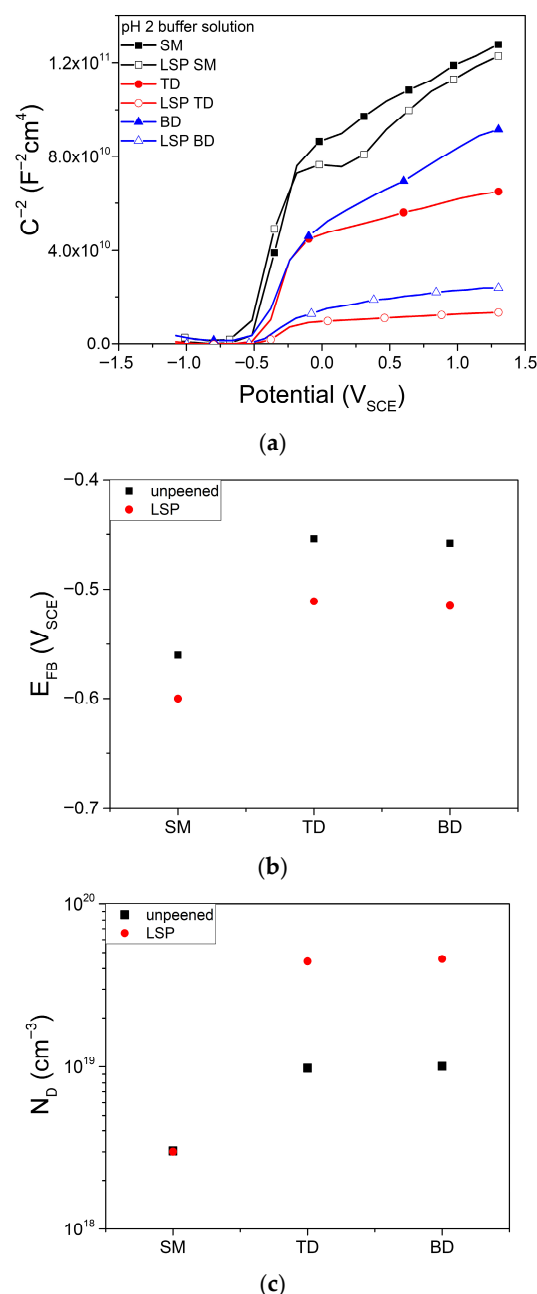


Figure 10. (a) Mott–Schottky plots, (b) donor concentration, and (c) flat-band potential of passive films on Ti-6Al-4V alloys in a pH 2 buffer solution.

N_d , which represents the concentration of oxygen vacancies in n-type passive films, is shown in Figure 10c. The N_d values for the passive film on the SM alloys were lower than that for the AM alloys and were largely unaffected by LSP. In contrast, the N_d values of the AM alloys increased significantly after LSP treatment. The potentiodynamic polarization curves (Figure 7) imply that V dissolved in the form of VO^{2+} or VO_2^+ , whereas Al did not undergo remarkable dissolution. This indicates that the passive film formed on the LSP-treated samples has fewer V^{4+} or V^{5+} ions compared with the film formed on the unpeened alloys. In general, ions with higher valence, such as V^{4+} and V^{5+} , can reduce the concentration of oxygen vacancies (VO^{2+}) in the passive film for charge balance if they substitute for Ti^{4+} in the TiO_2 lattice. Therefore, the unpeened specimens, possibly with higher concentrations of V^{4+} and V^{5+} species, are likely to form less defective passive films.

The high concentration of point defects may contribute to the high passive current density observed for the LSP-treated alloys, as shown in Figure 9. However, N_d alone cannot

explain the high current density. For example, although the unpeened BD alloy showed a current density comparable to that the SM alloys (Figure 9), its N_d was considerably larger, similar to that of the TD alloy. The passive current density is governed by the flux of point defects, which depends on both the concentration and diffusivity of these defects [89].

It is proposed that the increase in N_d after LSP in the AM alloys may be associated with the dissolution of V from the supersaturated α' phase, as evidenced by the anodic peaks observed in the potentiodynamic polarization curves (Figure 7). The release of V species from the passive film may influence the defect structure of the film, potentially increasing the concentration of oxygen vacancies. According to the point defect model [55], an increase in oxygen vacancy concentration can enhance defect transport through the passive film, which may contribute to the reduced stability of the passive film. This interpretation is consistent with the higher i_{ss} and Q_{final} values observed in the LSP-treated AM specimens. However, it should be noted that this proposed mechanism is based on indirect electrochemical evidence, and direct verification of passive film composition, for example, by X-ray photoelectron spectroscopy, would be required to confirm this hypothesis.

Nevertheless, based on the general consistency in the trends of the passive current density in Figure 9 and N_d in Figure 10c, it can be inferred that a higher defect density leads to reduced protectiveness of the passive film. These results suggest that the diffusion coefficients of the vacancies in the passive films were not significantly changed by AM or LSP. Further work is required to elucidate the passivity of AM alloys under surface treatments, such as LSP, especially for BD samples that exhibit lower passive current densities than would be expected based on the N_d value.

4. Conclusions

The effects of LSP on the passivity of SM Ti–6Al–4V and AM Ti–6Al–4V alloys were investigated, and the following conclusions were derived.

1. LSP increased the surface roughness ($Ra \approx 0.25$ to $0.6 \mu\text{m}$), enhanced surface hardness by 12–16%, and introduced compressive residual stresses ranging from -450 to -950 MPa in both alloys. After LSP, the SM alloy exhibited β -phase enrichment and grain refinement, whereas the AM alloy showed a decrease in the α' phase.
2. All specimens showed an active–passive transition after LSP, and the corrosion rate decreased from $\sim 5 \times 10^{-6}$ to $\sim 1 \times 10^{-6} \text{ A}\cdot\text{cm}^{-2}$. The introduction of compressive residual stress reduced the corrosion rate, despite the increased surface roughness.
3. During 24 h potentiostatic polarization at $1.3 V_{SCE}$, the current density of LSP AM specimens remained higher than that of their unpeened counterparts, whereas the LSP SM specimens showed current densities comparable to those of the other samples. These findings indicate that LSP effectively reduces the corrosion rate but may degrade the long-term passive film stability of AM Ti–6Al–4V alloys.
4. Potentiodynamic polarization results suggest that the behavior of SM and AM alloys is controlled by different anodic reactions. In the SM alloy, a rapid anodic process leads to a decrease in the corrosion potential, whereas in the AM alloy, a distinct anodic behavior delays passivation and increases the corrosion potential.
5. According to the Mott–Schottky analysis, the donor density of the passive films on SM specimens was lower than that of the AM specimens and changed marginally after LSP. In contrast, the donor density of the AM specimens was significantly increased by LSP, which increased the number of oxygen vacancies and decreased the stability of the passive films.

Author Contributions: Conceptualization, T.M., J.B. and H.J.; Methodology, J.K., M.D., T.M., J.B. and H.J.; Formal analysis, J.L.; Investigation, J.L., J.K. and M.D.; Data curation, J.L.; Writing—

original draft, J.L.; Writing—review & editing, H.J.; Visualization, J.L.; Supervision, H.J.; Project administration, H.J.; Funding acquisition, H.J. All authors have read and agreed to the published version of the manuscript.

Funding: This research was supported by a National Research Foundation of Korea (NRF) grant funded by the Korean Government (MSIT) (No. RS-2023-NR076526) and the Ministry of Science and ICT under government funding (No. RS-2023-00217415). This work was also co-funded by the European Union and the state budget of the Czech Republic under the project LasApp (CZ.02.01.01/00/22_008/0004573).

Data Availability Statement: The original contributions presented in this study are included in the article. Further inquiries can be directed to the corresponding author.

Conflicts of Interest: The authors declare no conflicts of interest.

References

- Madigan, C.S.; Vaddula, A.; Yerramsetti, S.D.; Buddaraju, K.M. Additive manufacturing of titanium and nickel-based superalloys: A review. *Mater. Today Proc.* **2023**. [CrossRef]
- Liu, Y.; Shi, J.; Wang, Y. Evolution, control, and mitigation of residual stresses in additively manufactured metallic materials: A review. *Adv. Eng. Mater.* **2023**, *25*, 2300489. [CrossRef]
- Park, S.; Kim, I.; Kim, Y.I.; Kim, D.K.; Oh, S.J.; Lee, K.A.; Lee, B. Residual stress analysis of additive manufactured A356.2 aluminum alloys using X-ray diffraction methods. *Korean J. Met. Mater.* **2023**, *61*, 534–544. [CrossRef]
- Lal, S. The enigma of titanium electrodeposition on various substrates. In *ECS Meeting Abstracts*; The Electrochemical Society: Philadelphia, PA, USA, 2023; Volume MA2023-02, p. 1249. [CrossRef]
- Besisa, N.H.A.; Yajima, T. Titanium-based alloys: Classification and diverse applications. In *Titanium-Based Alloys—Characteristics and Applications*; Vizureanu, P., Baltatu, M.S., Eds.; IntechOpen: London, UK, 2024. [CrossRef]
- Baltatu, M.S.; Vizureanu, P.; Sandu, A.V.; Achitei, D.C.; Perju, M.C.; Burduhos-Nergis, D.D.; Benchea, M. Ti-tanium—A versatile metal in modern applications. In *Titanium-Based Alloys—Characteristics and Applications*; Vizureanu, P., Baltatu, M.S., Eds.; IntechOpen: London, UK, 2024. [CrossRef]
- Wu, H.; Chen, X.; Kong, L.; Liu, P. Mechanical and biological properties of titanium and its alloys for oral implant with preparation techniques: A review. *Materials* **2023**, *16*, 6860. [CrossRef]
- Guo, S.; Song, Y.; Wu, Y.; Hu, J.; Lu, J.; Wang, C.; Jia, Z.; Hua, L. Microscopic mechanism of enhanced strength–plasticity synergy in pre-damaged TC11 titanium alloys via novel electroshock treatment. *J. Alloys Compd.* **2026**, *1052*, 186139. [CrossRef]
- Chen, Y.; Fu, J.; Zhou, L.; Zhao, Y.; Wang, F.; Chen, G.; Qin, Y. Effect of heat treatment on microstructure and mechanical properties of titanium alloy fabricated by laser–arc hybrid additive manufacturing. *Coatings* **2024**, *14*, 614. [CrossRef]
- Tebianian, M.; Aghaie, S.; Jafari, N.S.R.; Hosseini, S.R.E.; Pereira, A.B.; Fernandes, F.A.O.; Farbakhti, M.; Chen, C.; Huo, Y. A review of the metal additive manufacturing processes. *Materials* **2023**, *16*, 7514. [CrossRef]
- Chen, Y. Cutting-edge additive manufacturing technology for titanium-based alloys. *Highlights Sci. Eng. Technol.* **2024**, *84*, 92–98. [CrossRef]
- Yumak, N. Post-processing heat treatment of titanium alloys manufactured by additive manufacturing technologies. In *Comprehensive Materials Processing*, 2nd ed.; Elsevier: Amsterdam, The Netherlands, 2024; Volume 11, pp. 221–232. [CrossRef]
- Fischer, D.; Cheng, K.-Y.; Neto, M.Q.; Hall, D.; Bijukumar, D.; Orías, A.A.E.; Pourzal, R.; Van Arkel, R.J.; Mathew, M.T. Corrosion behavior of selective laser melting (SLM) manufactured Ti6Al4V alloy in saline and BCS solution. *J. Bio-Tribo-Corros.* **2022**, *8*, 63. [CrossRef] [PubMed]
- Tsuchiya, H.; Miyabe, S.; Doi, K.; Fujimoto, S. Corrosion resistance of titanium—Localized corrosion and galvanic corrosion. *J. Surf. Finish. Soc. Jpn.* **2022**, *73*, 33–37. [CrossRef]
- Yarram, A.; Ramesh, K.S.V.; Narasimha Rao, G.; Yasmeen, S.A.; Suresh Sajjan, M.C.; Ramaraju, A.V. Corrosion in titanium dental implants—A review. *Int. J. Dent. Mater.* **2019**, *1*, 72–78. [CrossRef]
- Yang, J.; Song, Y.; Dong, K.; Han, E.-H. Research progress on the corrosion behavior of titanium alloys. *Corros. Rev.* **2023**, *41*, 5–20. [CrossRef]
- Jayaraj, J.; Ranjith, P.M.; Ningshen, S.; Ramanathan, S. Studies on corrosion of titanium and air-oxidized titanium in fluorinated nitric acid. *Trans. Indian Inst. Met.* **2019**, *72*, 1917–1926. [CrossRef]
- Kurtz, M.A.; Alaniz, K.; Kurtz, P.W.; Wessinger, A.C.; Moreno-Reyes, A.; Gilbert, J.L. Oxide degradation precedes additively manufactured Ti-6Al-4V selective dissolution: An unsupervised machine learning correlation of impedance and dissolution compared to Ti-29Nb-21Zr. *J. Biomed. Mater. Res. A* **2024**, *112*, 1250–1264. [CrossRef]

19. Lavrys, S.; Pohrel'yuk, I.; Veselivska, H.; Skrebtsov, A.; Kononenko, J.; Marchenko, Y. Corrosion behavior of near-alpha titanium alloy fabricated by additive manufacturing. *Mater. Corros.* **2022**, *73*, 2063–2070. [CrossRef]
20. Yu, Z.; Chen, Z.; Qu, D.; Qu, S.; Wang, H.; Zhao, F.; Zhang, C.; Feng, A.; Chen, D. Microstructure and electrochemical behavior of a 3D-printed Ti-6Al-4V alloy. *Materials* **2022**, *15*, 4473. [CrossRef]
21. Lee, J.-B.; Seo, D.-I.; Chang, H.-Y. Evaluating corrosion resistance of biomedical Ti-6Al-4V alloys fabricated via additive manufacturing using electrochemical critical localized corrosion potential. *Met. Mater. Int.* **2021**, *27*, 2353–2359. Correction in *Met. Mater. Int.* **2021**, *27*, 3095. <https://doi.org/10.1007/s12540-021-01085-5>. [CrossRef]
22. Lee, J.-B.; Seo, D.-I.; Chang, H.-Y. Evaluating corrosion resistance of additive-manufactured Ti-6Al-4V using electrochemical critical localized corrosion temperature. *Met. Mater. Int.* **2020**, *26*, 39–45. [CrossRef]
23. Kalentics, N.; Boillat, E.; Peyre, P.; Ćirić-Kostić, S.; Bogojević, N.; Logé, R.E. Tailoring residual stress profile of selective laser melted parts by laser shock peening. *Addit. Manuf.* **2017**, *16*, 90–97. [CrossRef]
24. Gel'atko, M.; Hatala, M.; Botko, F.; Vandžura, R.; Hajnyš, J.; Šajgalík, M.; Török, J. Stress relieving heat treatment of 316L stainless steel made by additive manufacturing process. *Materials* **2023**, *16*, 6461. [CrossRef]
25. De Baere, D.; Van Cauwenbergh, P.; Bayat, M.; Mohanty, S.; Thorborg, J.; Thijs, L.; Van Hooreweder, B.; Vanmeensel, K.; Hattel, J.H. Thermo-mechanical modelling of stress relief heat treatments after laser-based powder bed fusion. *Addit. Manuf.* **2021**, *38*, 101818. [CrossRef]
26. Zha, X.-Q.; Xiong, Y.; Zhou, T.; Ren, Y.-F.; Hei, P.-H.; Zhai, Z.-L.; Kömi, J.; Huttula, M.; Cao, W. Impacts of stress relief treatments on microstructure, mechanical and corrosion properties of metal active-gas welding joint of 2205 duplex stainless steel. *Materials* **2020**, *13*, 4272. [CrossRef]
27. Peyre, P.; Scherpereel, X.; Berthe, L.; Carboni, C.; Fabbro, G.; Béranger, G.; Lemaitre, C. Surface modifications induced in 316L steel by laser peening and shot-peening. Influence on pitting corrosion resistance. *Mater. Sci. Eng. A* **2000**, *280*, 294–302. [CrossRef]
28. Cai, J.; Wu, H.; Tian, Y.; Zhang, X. The influence of ultrasonic shot peening on the microstructure and fatigue behavior of TC17 alloy. *Sci. Rep.* **2025**, *15*, 13548. [CrossRef] [PubMed]
29. Chen, H.; Guan, Y.; Zhu, L.; Li, Y.; Zhai, J.; Lin, J. Effects of ultrasonic shot peening process parameters on nanocrystalline and mechanical properties of pure copper surface. *Mater. Chem. Phys.* **2021**, *259*, 124025. [CrossRef]
30. Sanseong, C.; Ro, J.-S.; Pyoung, Y.-S.; Amanov, A. Effects of high-temperature UNSM treatment on wear re-sistance of Ti-6Al-4V alloy prepared by selective laser melting. *Tribol. Lubr.* **2020**, *36*, 47–54. [CrossRef]
31. Cho, H.; Yoo, Y.-R.; Kim, Y.-S. Effect of ultrasonic nanocrystalline surface modification (UNSM) on stress corrosion cracking of 304L stainless steel. *Metals* **2024**, *14*, 1315. [CrossRef]
32. Wei, S.; Kaimini, L.; Wanjia, L.; Wanwu, D. Effect of fretting wear on TC4 alloy prepared by laser shock peening at high temperature. *Surf. Eng.* **2024**, *40*, 112–124. [CrossRef]
33. Zhang, Y.; Peng, L.; Wang, Y.; Ye, C. Improving surface integrity and wear resistance of selective laser melted 316L stainless steel using ultrasonic nanocrystal surface modification. *Procedia CIRP* **2024**, *123*, 481–486. [CrossRef]
34. Yakin, R.I.; Iswanto, P.T.; Maliwemu, E.U.K. Shot peening effect on surface properties and pitting corrosion resistance of biomedical structural steel AISI 316L. *Metalurgija* **2021**, *60*, 249–252.
35. Cho, H.; Yoo, Y.-R.; Kim, Y.-S. Effect of ultrasonic shot peening on microstructure and corrosion properties of GTA-welded 304L stainless steel. *Crystals* **2024**, *14*, 531. [CrossRef]
36. Luo, G.; Zhang, J.; Xiong, Y.; Zhang, B.; Chen, X.; Wu, Y.; Wang, S.; Cao, W. Effect of laser shock peening on the corrosion properties of Ti-6Al-3Nb-2Zr-1Mo alloy. *Surf. Coat. Technol.* **2022**, *440*, 128425. [CrossRef]
37. Jiang, L.; Lan, L.; Wang, H.; Yan, X.; Gao, S.; He, B.; Chen, C. Laser shock peening of laser melting deposited TiAl alloy for enhancing its corrosion resistance. *Surf. Coat. Technol.* **2024**, *483*, 130745. [CrossRef]
38. Chattopadhyay, A.; Muvvala, G.; Sarkar, S.; Racherla, V.; Nath, A.K. Effect of laser shock peening on micro-structural, mechanical and corrosion properties of laser beam welded commercially pure titanium. *Opt. Laser Technol.* **2021**, *133*, 106527. [CrossRef]
39. Gujba, A.K.; Medraj, M. Laser peening process and its impact on materials properties in comparison with shot peening and ultrasonic impact peening. *Materials* **2014**, *7*, 7925–7974. [CrossRef] [PubMed]
40. Deng, W.; Wang, C.; Lu, H.; Meng, X.; Wang, Z.; Lv, J.; Luo, K.; Lu, J. Progressive developments, challenges and future trends in laser shock peening of metallic materials and alloys: A comprehensive review. *Int. J. Mach. Tools Manuf.* **2023**, *191*, 104061. [CrossRef]
41. Kaufman, J.; Racek, J.; Cieslar, M.; Minárik, P.; Steiner, M.A.; Mannava, S.R.; Vasudevan, V.K.; Sharma, A.; Böhm, M.; Brajer, J.; et al. The effect of laser shock peening with and without protective coating on intergranular corrosion of sensitized AA5083. *Corros. Sci.* **2022**, *194*, 109925. [CrossRef]
42. Khezri, M.K.; Moghaddam, A.; Ahmadi-Brooghani, S.Y. Effect of laser shock peening on the stress corrosion cracking of Inconel 792. *J. Mater. Eng. Perform.* **2026**. [CrossRef]
43. Xiong, Y.; Shen, Y.; He, L.; Yang, Z.; Song, R. Stress corrosion cracking behavior of LSP/MAO treated magnesium alloy during SSRT in a simulated body fluid. *J. Alloys Compd.* **2020**, *822*, 153707. [CrossRef]

44. Guan, L.; Li, Y.; Liao, L.; Xia, D.; Zhong, J.; Zheng, Z.; Fu, H.; Shi, L.; Wang, G. Improvement of electrochemical corrosion uniformity in AA2024 FSW joints by laser shock peening. *J. Mater. Res. Technol.* **2026**, *41*, 2183–2192. [\[CrossRef\]](#)
45. Abeens, M.; Muruganandhan, R.; Thirumavalavan, K. Effect of low energy laser shock peening on plastic deformation, wettability and corrosion resistance of aluminum alloy 7075 T651. *Optik* **2020**, *219*, 165045. [\[CrossRef\]](#)
46. Karthik, D.; Deshmukh, K.; Praveenkumar, K.; Swaroop, S. Laser peening induced mitigation of severe pitting corrosion in titanium stabilized 321 steel. *Opt. Laser Technol.* **2024**, *172*, 110537. [\[CrossRef\]](#)
47. Karthik, D.; Jiang, J.; Hu, Y.; Yao, Z. Effect of multiple laser shock peening on microstructure, crystallo-graphic texture and pitting corrosion of aluminum–lithium alloy 2060-T8. *Surf. Coat. Technol.* **2021**, *421*, 127354. [\[CrossRef\]](#)
48. Chierchia, R.; Menchini, F.; Serenelli, L.; Mangiapane, P.; Polichetti, T.; Tucci, M. Titanium oxide films de-positied by e-beam evaporation as n-type electrode for solar cell applications. *Phys. Status Solidi C* **2016**, *13*, 1002–1005. [\[CrossRef\]](#)
49. Zeng, Z.-L. First-principles study on the structural and electronic properties of N atoms doped-rutile TiO₂ of oxygen vacancies. *Adv. Mater. Sci. Eng.* **2015**, *2015*, 670243. [\[CrossRef\]](#)
50. Azumi, K.; Ohtsuka, T. Impedance study of semiconductor property of the passive film on titanium. *Corros. Eng.* **1997**, *46*, 169–175. [\[CrossRef\]](#)
51. Dai, N.; Zhang, L.-C.; Zhang, J.; Chen, Q.; Wu, M. Corrosion behavior of selective laser melted Ti–6Al–4V alloy in NaCl solution. *Corros. Sci.* **2016**, *102*, 484–489. [\[CrossRef\]](#)
52. Dai, N.; Zhang, L.-C.; Zhang, J.; Zhang, X.; Ni, Q.; Chen, Y.; Wu, M.; Yang, C. Distinction in corrosion re-sistance of selective laser melted Ti–6Al–4V alloy on different planes. *Corros. Sci.* **2016**, *111*, 703–710. [\[CrossRef\]](#)
53. Dai, N.; Zhang, J.; Chen, Y.; Zhang, L.-C. Heat treatment degrading the corrosion resistance of selective la-ser melted Ti–6Al–4V alloy. *J. Electrochem. Soc.* **2017**, *164*, C428–C434. [\[CrossRef\]](#)
54. Zhan, Z.; Zhang, Q.; Wang, S.; Liu, X.; Zhang, H.; Sun, Z.; Ge, Y.; Du, N. Comparison on the electrochemical corrosion behavior of Ti6Al4V alloys fabricated by laser powder bed fusion and casting. *Materials* **2024**, *17*, 3322. [\[CrossRef\]](#) [\[PubMed\]](#)
55. Macdonald, D.D. Passivity—The key to our metals-based civilization. *Pure Appl. Chem.* **1999**, *71*, 951–978. [\[CrossRef\]](#)
56. Jang, H.; Kwon, H.S. In situ study on the effects of Ni and Mo on the passive film formed on Fe–20Cr alloys by photoelectrochemical and Mott–Schottky techniques. *J. Electroanal. Chem.* **2006**, *590*, 120–125. [\[CrossRef\]](#)
57. Jang, H.; Oh, K.-N.; Ahn, S.; Kwon, H.S. Determination of the diffusivity of cation vacancy in a passive film of Ni using Mott–Schottky analysis and in-situ ellipsometry. *Met. Mater. Int.* **2014**, *20*, 277–283. [\[CrossRef\]](#)
58. Seo, D.-I.; Lee, J.-B. Measurement of localized corrosion resistance in additively manufactured Ti-6Al-4V alloys using electrochemical critical localized corrosion temperature (E-CLCT) versus electrochemical critical local-ized corrosion potential (E-CLCP). *Corros. Sci. Technol.* **2021**, *20*, 37–43. [\[CrossRef\]](#)
59. Case, R.; Castaneda, H.; Ding, Y.; Khan, A.; Cedeno-Vente, M.L.; Peña, G. Evaluation of the relationship between passivity and microstructure in austenitic stainless steel, the point defect perspective. In *Proceedings of the AMPP Annual Conference + Expo 2023*; Paper No. AMPP-2023-19344; Association for Materials Protection and Performance (AMPP): Houston, TX, USA, 2023. [\[CrossRef\]](#)
60. Guo, P.; Lin, X.; Macdonald, D.D.; Odneval, I.; Zhang, S.; Zhang, Y.; Lin, C.; Wu, Q.; Yang, Y.; Huang, W. Chloride induced secondary passive film failure for laser additive manufacturing nickel-based superalloys during electrochemical machining. *J. Electrochem. Soc.* **2023**, *170*, 063508. [\[CrossRef\]](#)
61. Madhan Kumar, A.; Toor, I.-u.-H. Localized corrosion evaluation of newly developed stainless-steel alloys in chloride medium through dynamic and localized micro electrochemical techniques. *J. Mater. Res. Technol.* **2023**, *26*, 5668–5682. [\[CrossRef\]](#)
62. Madhan Kumar, A.; Toor, I.-u.-H. Dynamic and localized microelectrochemical approaches to evaluate the corrosion resistance of newly developed lean duplex stainless steel alloys. *Mater. Corros.* **2022**, *73*, 1687–1700. [\[CrossRef\]](#)
63. Mason, P.; Divoký, M.; Ertel, K.; Pilar, J.; Butcher, T.; Hanuš, M.; Banerjee, S.; Phillips, J.; Smith, J.; De Vido, M.; et al. Kilowatt average power 100 J-level diode pumped solid state laser. *Optica* **2017**, *4*, 438–439. [\[CrossRef\]](#)
64. Ji, F.; Liu, R.; Wang, Z.; Liu, J.; Guan, L.; Liu, Z.; Bai, Y. The mechanical coupling effect of α and β phases in Ti6Al4V alloy undergoing laser shock peening: A molecular dynamics study. *Mater. Sci. Eng. A* **2024**, *915*, 147208. [\[CrossRef\]](#)
65. Wu, J.; Liu, H.; Wei, P.; Zhu, C.; Lin, Q. Effect of shot peening coverage on hardness, residual stress and surface morphology of carburized rollers. *Surf. Coat. Technol.* **2020**, *384*, 125273. [\[CrossRef\]](#)
66. Feng, X.-W.; Xie, J.; Xue, W.-Y.; Shen, Y.-F.; Wang, H.-B.; Liu, Z.-Y. Microstructure and nanoindentation hardness of shot-peened ultrafine-grained low-alloy steel. *J. Iron Steel Res. Int.* **2019**, *26*, 472–482. [\[CrossRef\]](#)
67. Li, K.J.; Zheng, Q.; Qin, Y.L.; Liu, X.W. Effect of shot peening on microstructure and properties of 34CrMo4 alloy. *Mater. Sci. Forum* **2018**, *934*, 105–110. [\[CrossRef\]](#)
68. Wang, C.; Wang, L.; Wang, C.-L.; Li, K.; Wang, X.-G. Dislocation density-based study of grain refinement induced by laser shock peening. *Opt. Laser Technol.* **2020**, *121*, 105827. [\[CrossRef\]](#)
69. Tao, H.; Xue, W.; Zhang, T.; Zhao, P.; Zhang, Z.; Zhang, B.; Wu, J. Effects of laser shock peening on the microstructural evolution and corrosion behavior of the new-generation high-strength Al–Zn–Mg–Cu alloy. *J. Alloys Compd.* **2026**, *1055*, 186425. [\[CrossRef\]](#)

70. Mironov, S.; Ozerov, M.; Kalinenko, A.; Stepanov, N.; Plekhov, O.; Sikhamov, R.; Ventzke, V.; Kashaev, N.; Salishchev, G.; Semiatin, L.; et al. On the relationship between microstructure and residual stress in laser-shock-peened Ti–6Al–4V. *J. Alloys Compd.* **2022**, *900*, 163383. [\[CrossRef\]](#)
71. Ho, A.; Zhao, H.; Fellowes, J.W.; Martina, F.; Davis, A.E.; Prangnell, P.B. On the origin of microstructural banding in Ti–6Al–4V wire-arc based high deposition rate additive manufacturing. *Acta Mater.* **2019**, *166*, 306–323. [\[CrossRef\]](#)
72. Zhou, L.; Pan, X.; Shi, X.; Du, T.; Wang, L.; Luo, S.; He, W.; Chen, P. Research on surface integrity of Ti–6Al–4V alloy with compound treatment of laser shock peening and shot peening. *Vacuum* **2022**, *196*, 110717. [\[CrossRef\]](#)
73. Wang, L.; Zhou, L.; Liu, L.; He, W.; Pan, X.; Nie, X.; Luo, S. Fatigue strength improvement in Ti–6Al–4V subjected to foreign object damage by combined treatment of laser shock peening and shot peening. *Int. J. Fatigue* **2022**, *155*, 106581. [\[CrossRef\]](#)
74. Gu, C.; Tian, Z.; Zhao, J.; Wang, Y. Investigation of microstructure and tribological property of Ti–6Al–4V alloy by laser shock peening processing. *Int. J. Adv. Manuf. Technol.* **2023**, *129*, 955–967. [\[CrossRef\]](#)
75. Nalla, R.K.; Altenberger, I.; Noster, U.; Liu, G.Y.; Scholtes, B.; Ritchie, R.O. On the influence of mechanical surface treatments—Deep rolling and laser shock peening—On the fatigue behavior of Ti–6Al–4V at ambient and elevated temperatures. *Mater. Sci. Eng. A* **2003**, *355*, 216–230. [\[CrossRef\]](#)
76. Schroeder, S.C.; Frankel, J.; Abbate, A. *The Relationship Between Residual Stress and Hardness and the Onset of Plastic Deformation*; Technical Report ARCCB-TR-95029; U.S. Army Armament Research, Development and Engineering Center: Watervliet, NY, USA, 1995.
77. Martina, F.; Roy, M.J.; Szost, B.A.; Terzi, S.; Colegrove, P.A.; Williams, S.W.; Withers, P.J.; Meyer, J.; Hofmann, M. Residual stress of as-deposited and rolled wire+arc additive manufacturing Ti–6Al–4V components. *Mater. Sci. Technol.* **2016**, *32*, 1439–1448. [\[CrossRef\]](#)
78. Bera, T.; Mohanty, S. A review on residual stress in metal additive manufacturing. *3D Print. Addit. Manuf.* **2024**, *11*, 1462–1470. [\[CrossRef\]](#) [\[PubMed\]](#)
79. Sotniczuk, A.; Dou, B.; Xie, C.; Tang, J.; Kalita, D.; Chromiński, W.; Garbacz, H.; Sun, F.; Ogle, K. New insights into the corrosion of orthopedic Ti–6Al–4V under cathodic polarization. *Corros. Sci.* **2024**, *238*, 112354. [\[CrossRef\]](#)
80. McCafferty, E. Thermodynamics of corrosion: Pourbaix diagrams. In *Introduction to Corrosion Science*; Springer: New York, NY, USA, 2010; pp. 95–117. [\[CrossRef\]](#)
81. Kokalj, A.; Ložinšek, M.; Kapun, B.; Taheri, P.; Neupane, S.; Losada-Pérez, P.; Xie, C.; Stavber, S.; Crespo, D.; Renner, F.U.; et al. Simplistic correlations between molecular electronic properties and inhibition efficiencies: Do they really exist? *Corros. Sci.* **2021**, *179*, 108856. [\[CrossRef\]](#)
82. Liu, X.; Frankel, G.S. Effects of compressive stress on localized corrosion in AA2024-T3. *Corros. Sci.* **2006**, *48*, 3309–3329. [\[CrossRef\]](#)
83. Seo, D.-I.; Lee, J.-B. Ti–6Al–4V alloy fabricated by additive manufacturing method using micro-droplet cell and critical pitting temperature techniques and evaluation of its resistance to corrosion. *Corros. Sci. Technol.* **2018**, *17*, 129–137. [\[CrossRef\]](#)
84. Ahn, K.; Jang, H. Effects of grinding and masking conditions on the potentiodynamic polarization curves of additively manufactured Ti–6Al–4V alloy in artificial saliva solution with or without fluoride ions. *Corros. Sci. Technol.* **2021**, *20*, 475–483. [\[CrossRef\]](#)
85. Wang, H.; Shu, X.; Zhao, J. Influence of build angle and polishing roughness on corrosion resistance of 316L stainless steel fabricated by SLM method. *Materials* **2022**, *15*, 4020. [\[CrossRef\]](#) [\[PubMed\]](#)
86. Vella, K.A.; Buhagiar, J.; Cassar, G.; Pizzuto, M.M.; Bonnici, L.; Chen, J.; Zhang, X.; Huang, Z.; Zammit, A. The effect of a duplex surface treatment on the corrosion and tribocorrosion characteristics of additively manufactured Ti–6Al–4V. *Materials* **2023**, *16*, 2098. [\[CrossRef\]](#)
87. Sajjad, U.; Abbas, A.; Sadeghianjahromi, A.; Abbas, N.; Liaw, J.-S.; Wang, C.-C. Enhancing corrosion resistance of Al 5050 alloy based on surface roughness and its fabrication methods; an experimental investigation. *J. Mater. Res. Technol.* **2021**, *11*, 1859–1867. [\[CrossRef\]](#)
88. Patel, M.Y.; Mortelliti, M.J.; Dempsey, J.L. A compendium and meta-analysis of flatband potentials for TiO₂, ZnO, and SnO₂ semiconductors in aqueous media. *Chem. Phys. Rev.* **2022**, *3*, 011303. [\[CrossRef\]](#)
89. Seo, D.-I.; Lee, J.-B. Localized corrosion and repassivation behaviors of additively manufactured titanium alloys in simulated biomedical solutions. *npj Mater. Degrad.* **2023**, *7*, 44. [\[CrossRef\]](#)

Disclaimer/Publisher’s Note: The statements, opinions and data contained in all publications are solely those of the individual author(s) and contributor(s) and not of MDPI and/or the editor(s). MDPI and/or the editor(s) disclaim responsibility for any injury to people or property resulting from any ideas, methods, instructions or products referred to in the content.